NEAT1 promotes genome stability via m⁶A methylation-dependent regulation of CHD4

Victoria Mamontova,[1,2] Barbara Trifault,[1,2] Anne-Sophie Gribling-Burrer,[3] Patrick Bohn,[3] Lea Boten,[1,2] Pit Preckwinkel,[4] Peter Gallant,[2] Daniel Solvie,[2] Carsten P. Ade,[2] Dimitrios Papadopoulos,[2] Martin Eilers,[2] Tony Gutschner,[4] Redmond P. Smyth,[3] and Kaspar Burger[1,2]

[1]Mildred Scheel Early Career Center for Cancer Research (Mildred-Scheel-Nachwuchszentrum [MSNZ]) Würzburg, University Hospital Würzburg, 97080 Würzburg, Germany; [2]Department of Biochemistry and Molecular Biology, Biocenter of the University of Würzburg, 97074 Würzburg, Germany; [3]Helmholtz Institute for RNA-Based Infection Research, Helmholtz-Center for Infection Research, 97808 Würzburg, Germany; [4]Department of RNA Biology and Pathogenesis, Institute of Molecular Medicine, Martin Luther University Halle-Wittenberg, Charles Tanford Protein Research Center, 06120 Halle, Germany

Long noncoding (lnc)RNAs emerge as regulators of genome stability. The nuclear-enriched abundant transcript 1 (NEAT1) is overexpressed in many tumors and is responsive to genotoxic stress. However, the mechanism that links NEAT1 to DNA damage response (DDR) is unclear. Here, we investigate the expression, modification, localization, and structure of NEAT1 in response to DNA double-strand breaks (DSBs). DNA damage increases the levels and N6-methyladenosine (m⁶A) marks on NEAT1, which promotes alterations in NEAT1 structure, accumulation of hypermethylated NEAT1 at promoter-associated DSBs, and DSB signaling. The depletion of NEAT1 impairs DSB focus formation and elevates DNA damage. The genome-protective role of NEAT1 is mediated by the RNA methyltransferase 3 (METTL3) and involves the release of the chromodomain helicase DNA binding protein 4 (CHD4) from NEAT1 to fine-tune histone acetylation at DSBs. Our data suggest a direct role for NEAT1 in DDR.

The DNA damage response (DDR) recognizes and repairs DNA lesions to prevent genome instability (Jackson and Bartek 2009; Ciccia and Elledge 2010). Unscheduled transcription exposes DNA and augments toxic DNA double-strand breaks (DSBs) (García-Muse and Aguilera 2019; Marnef and Legube 2021). DSB repair (DSBR) is governed by kinases like ataxia telangiectasia mutated (ATM) that activate >100 factors to amplify DDR and impair transcription (Kastan and Lim 2000; Blackford and Jackson 2017; Caron et al. 2019; Machour and Ayoub 2020). Interestingly, DSB-responsive kinases modify many RNA binding proteins (RBPs), suggesting a cross-talk of DDR with RNA metabolism (Dutertre et al. 2014; Burger et al. 2019a; Klaric et al. 2021). The production and processing of noncoding transcripts indeed facilitates RNA templated repair or scaffolds the recruitment of DSBR factors to stimulate canonical DDR (Chowdhury et al. 2013;

Burger et al. 2017, 2019b; Michelini et al. 2018; Zong et al. 2020).

Paraspeckles are nuclear bodies that condensate around two isoforms of the long noncoding RNA (lncRNA) nuclear-enriched abundant transcript 1 (NEAT1). The nuclear, non-poly-A-tailed NEAT1_2 isoform tethers >40 RBPs to paraspeckles and modulates RNA metabolism, whereas cytoplasmic, poly-A-tailed NEAT1_1 stimulates glycolysis (Fox et al. 2018; Hirose et al. 2023; Mattick et al. 2023). Thus, NEAT1 both promotes tumorigenesis and is tumor-suppressive, suggesting a dual role in cancer (Mello et al. 2017; Klec et al. 2019; Pisani and Baron 2020). Intriguingly, DDR elevates NEAT1 levels to promote genome stability (Adriaens et al. 2016). However, mechanistic insight into NEAT1-dependent DDR is sparse. Here, we show that NEAT1 accumulates at promoter-associated DSBs to foster genome stability in human U2OS osteosarcoma cells. NEAT1 chromatin occupancy depends on the RNA methyltransferase 3 (METTL3), which places

Corresponding author: kaspar.burger@uni-wuerzburg.de

N6-methyladenosine (m^6A) marks on NEAT1 to enhance NEAT1 association with DSBs. Hypermethylation of NEAT1 is accompanied by structural changes and releases the histone deacetylase CHD4 to fine-tune histone acetylation. The depletion of NEAT1 in turn elevates DNA damage and impairs DSB signaling, suggesting a genome-protective role for NEAT1.

Results

DNA damage induces NEAT1 expression

We hypothesized that high levels of NEAT1 protect tumor cells from excessive DNA damage. We therefore used RT-qPCR and RNA fluorescent in situ hybridization (FISH) to initially quantify the bulk of NEAT1 (isoform-overlapping transcripts, referred to here as NEAT1) and NEAT1_2 in U2OS cells. Treatment with the topoisomerase II inhibitor etoposide elevated nuclear but not cytoplasmic NEAT1 and NEAT1_2 levels (Fig. 1A,B; Supplemental Fig. S1A,B). The induction of DNA damage was confirmed by probing for the DNA damage marker phospho-Ser-139 histone H2A.X (γH2A.X) and the DNA damage-inducible lncRNA DINO (Supplemental Fig. S1C,D). Using our published 4sU-seq data on nascent RNA synthesis (Trifault et al. 2024), we found elevated synthesis of NEAT1_2 transcripts upon etoposide treatment, which was confirmed by
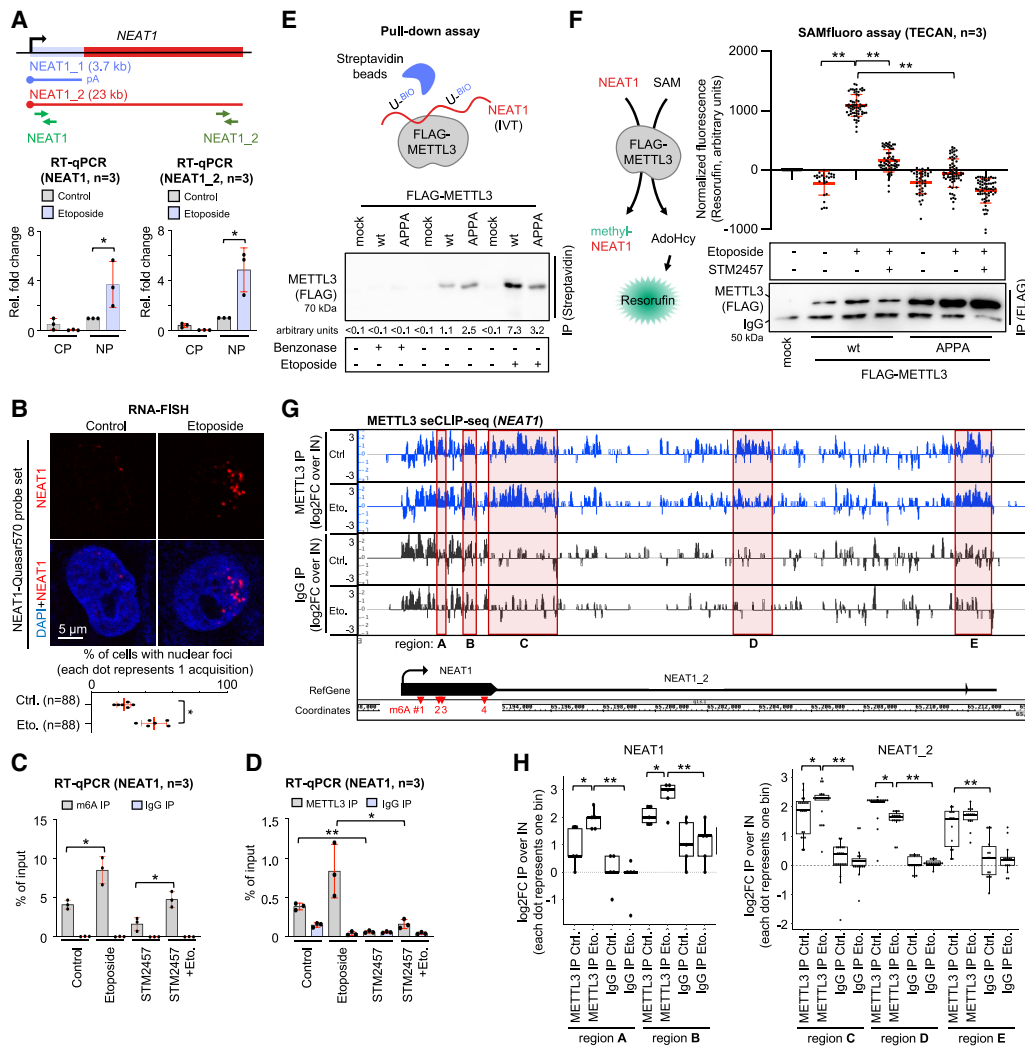

Figure 1. METTL3 stabilizes NEAT1 upon DNA damage in U2OS cells. (*A*) Scheme (*top*) and RT-qPCR (*bottom*) to assess NEAT1 levels in subcellular fractions. (CP) Cytoplasm, (NP) nucleoplasm, (green) primer site (pA) poly-A tail. (*B*) Imaging (*top*) and quantitation (*bottom*) of RNA-FISH signals. (*C,D*) RT-qPCR assessing NEAT1 upon m^6A immunoprecipitation (IP) from total RNA (*C*) or METTL3 IP from lysates (*D*). IgG was used as the control. (*E*) Scheme of pull-down assay (*top*) and immunoblot (*bottom*) displaying ectopically expressed FLAG-tagged METTL3 variants upon IP with biotin (BIO)-labeled, immobilized NEAT1 in vitro transcription (IVT) product. (Mock) Nontransfected control. (*F*) Scheme of SAMfluoro assay (*left*) and fluorescent counts displaying Resorufin levels (*top right*) and FLAG-METTL3 variants (immunoblot; *bottom right*). (SAM) S-adenosyl-L-methionine, (AdoHcy) S-adenosyl-L-homocysteine. (*G,H*) Browser tracks (*G*) and quantitation (*H*) of METTL3 seCLIP-seq reads. (Red box) Region of interest, (arrowhead) transcription start site, (dashed line) background, (red arrowhead) m^6A site. (*) P-value < 0.05, (**) P < 0.001; two-tailed t-test. Error bar indicates mean ± SD. (n) Number of replicates or cells.

RNA-FISH (Supplemental Fig. S1E,F). To assess the level of poly-A-tailed NEAT1_1, we used RT-qPCR and quantified NEAT1 cDNA (isoform-overlapping sequence) upon reverse transcription with either random hexamer or oligo-dT primers. The latter was approximately fourfold less abundant irrespective of etoposide treatment (Supplemental Fig. S1G). Thus, etoposide treatment induces NEAT1_2 in U2OS cells.

METTL3 binds and methylates NEAT1 upon DNA damage

The RNA methyltransferase 3 (METTL3) accumulates at DSBs and places m^6A marks on stress-responsive transcripts like NEAT1 (Wen et al. 2020; Zhang et al. 2020; Raj et al. 2022). We speculated that METTL3-dependent m^6A methylation stabilizes NEAT1 upon DNA damage. First, we used proximity ligation assays (PLAs) and dot blotting to confirm that etoposide both induces colocalization of METTL3 with γH2A.X-positive DSB foci in an ATM-dependent manner and elevates m^6A marks on total RNA (Supplemental Fig. S1H,I). To assess m^6A marks on NEAT1, we next used an m^6A antibody for immunoprecipitation (IP) of transcripts from intact total RNA samples and quantified NEAT1 levels by RT-qPCR (Fig. 1C; Supplemental Fig. S2A,B). NEAT1 coenrichment was detectable in untreated controls, pronounced upon etoposide treatment, and attenuated after preincubation with the METTL3 inhibitor STM2457 (Yankova et al. 2021). Next, we performed METTL3 IP to test whether NEAT1 differentially associates with METTL3 upon DNA damage. Indeed, NEAT1 prominently coenriched with METTL3 upon etoposide treatment but not STM2457 preincubation (Fig. 1D; Supplemental Fig. S2C). The METTL3 inhibitor also prevented the etoposide-responsive increase in NEAT1 levels (Supplemental Fig. S2D). To test whether METTL3 binds NEAT1, we incubated in vitro transcribed, biotinylated and bead-immobilized NEAT1 (isoform-overlapping sequence) with lysates from HEK293 cells that expressed wild-type (wt) FLAG-METTL3 or a catalytically inactive mutant (APPA) in the absence or presence of etoposide. NEAT1 pull-down prominently coenriched wt but not APPA FLAG-METTL3 from lysates of etoposide-treated cells (Fig. 1E). Next, we incubated in vitro transcribed, nonmethylated NEAT1 with immunoselected FLAG-METTL3 variants and performed a fluorescence-based in vitro methylation assay (Fig. 1F). We measured elevated levels of the reaction product Resorufin, indicating increased substrate methylation upon IP of wt but not APPA FLAG-METTL3 from lysates of etoposide-treated cells. Importantly, the production of Resorufin was sensitive to STM2457. The integrity of the assay was further confirmed by immunoblotting and gel electrophoresis (Supplemental Fig. S2E,F). Next, we performed METTL3 seCLIP-seq and determined five regions of METTL3 binding across NEAT1 (Fig. 1G, H). Etoposide treatment increased METTL3 binding at regions A and B (isoform-overlapping sequence) and region C (proximal part of NEAT1_2) but not at regions D and E (middle and distal parts of NEAT1_2). Interestingly, the NEAT1 isoform-overlapping sequence harbors four m^6A

sites with a DRACH consensus motif that are methylated by METTL3 (Wen et al. 2020). As those sites overlap or are close to the etoposide-responsive METTL3 binding regions A–C, we conclude that NEAT1 is bound by METTL3 and is hypermethylated upon DNA damage.

NEAT1 depletion impairs DDR

To test whether METTL3 and NEAT1 cooperate upon DNA damage, we assessed the amount of DSBs by neutral comet assay, which detects fast-migrating DSB-induced DNA fragments as tails upon release from the nucleus. We detected an etoposide-induced tail phenotype that was enhanced upon siRNA-based knockdown of either NEAT1 or METTL3 and most prominently observed upon codepletion of both factors (Fig. 2A,B). RNAi efficacy was monitored by RT-qPCR and immunoblotting (Supplemental Fig. S3A,B). Next, we applied an etoposide pulse-chase protocol to assess the impact of NEAT1 depletion on the formation and clearance of p53 binding protein 1 (53BP1)-positive DSB foci (Fig. 2C,D). Confocal imaging revealed that NEAT1 depletion impaired the formation of such foci. We also used antisense oligonucleotides (ASOs) to selectively deplete NEAT1_2 and observed impaired formation of γH2A.X marks, as well as reduced phosphorylation of checkpoint kinase 2 (CHK2) and other substrates of ATM but not ATM itself, upon pulse-chase treatment with etoposide (Fig. 2E; Supplemental Fig. S3C–E), suggesting defects in DSB signaling in NEAT1-deficient cells. Of note, ASO transfection did not cause accumulation of NEAT1 isoform-overlapping transcripts or perturb the cell cycle (Supplemental Fig. S3C,F). Next, we quantified DSBs genome-wide by BLISS and found that etoposide induces DSBs at both promoter regions and transcription end sites, and that the former significantly increase upon NEAT1 depletion (Fig. 2F). We also used U2OS DIvA cells as an orthogonal system for DSB induction. DIvA cells stably express the endonuclease AsiSI to produce ~80 locus-specific DSBs in the presence of 4-hydroxytamoxifen (4-OHT) (Supplemental Fig. S4A; Clouaire et al. 2018). We confirmed the induction of NEAT1_2 in DIvA cells by RT-qPCR and imaging and also validated the formation of DSB markers by immunoblotting and imaging (Supplemental Fig. S4B–E). As some DSB foci formed in untreated DIvA cells, we subsequently used wt U2OS cells as a control. We performed ChIP for γH2A.X at the promoter-associated AsiSI site DS1 for further validation. As expected, AsiSI cleavage triggered the formation of γH2A.X marks up to 2 kb upstream of DS1 (Supplemental Fig. S4F). Using ChIP, we observed that NEAT1 depletion weakened the formation of γH2A.X marks but increased signals for the upstream DSB markers Nibrin (NBS1) and histone H2B lys-120 acetylation (H2B120ac) in DIvA cells (Fig. 2G–I). We conclude that NEAT1 promotes efficient DSB signaling.

NEAT1 accumulates at DSBs

NEAT1 associates with >100 promoters in unperturbed cells (West et al. 2014). We reasoned that DDR alters
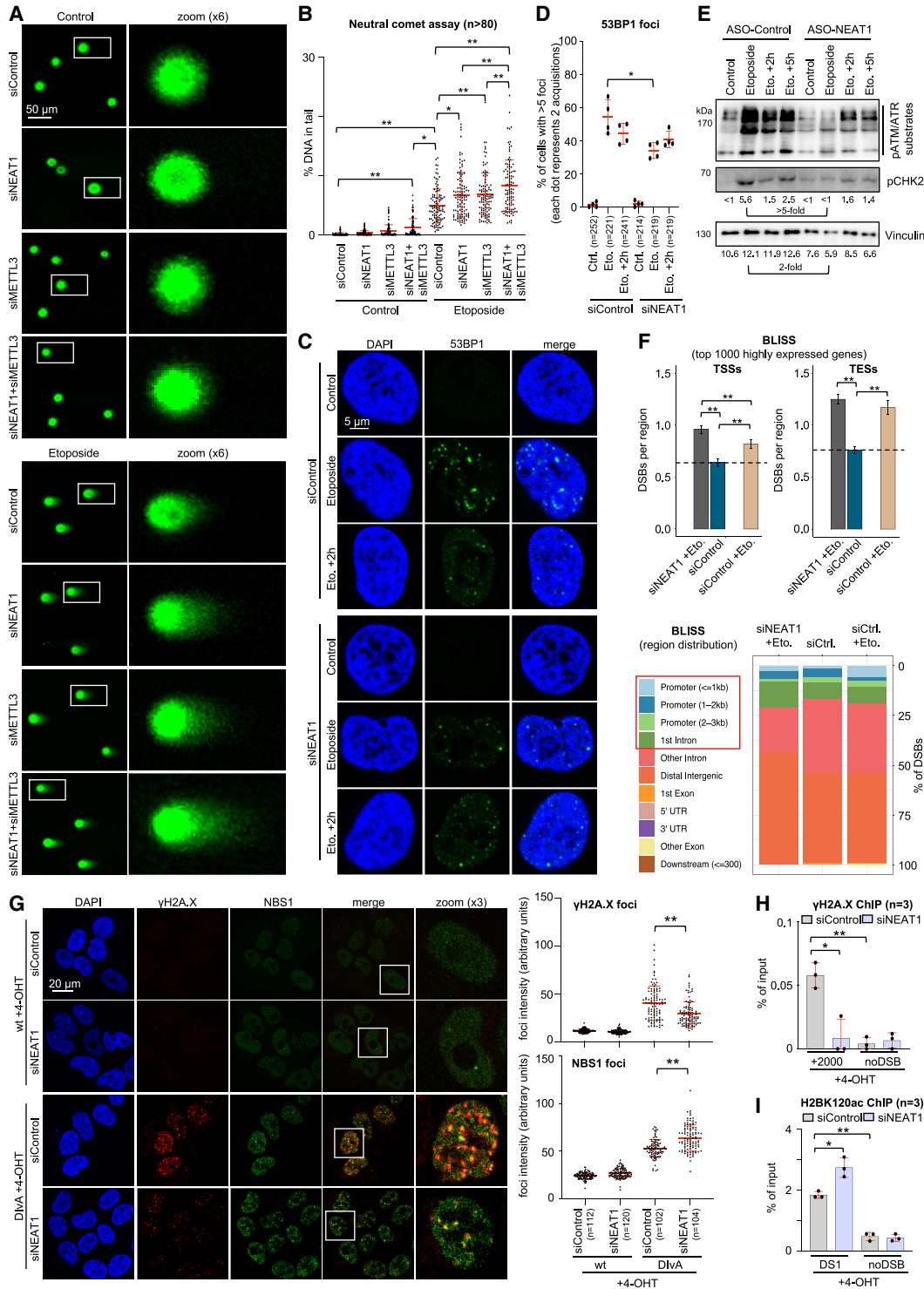
Figure 2. NEAT1 depletion elevates DNA damage and impairs DSB signaling in U2OS cells. (*A,B*) Imaging (*A*) and quantitation (*B*) of neutral comet assay displaying SYBR Gold-stained DNA. (White box) Zoom. (*C,D*) Imaging (*C*) and quantitation (*D*) of 53BP1 signals upon etoposide treatment and chase (Eto. +2 h). (*E*) Immunoblots for phospho-(p)ATM/ATR substrates and phospho-Thr-68 checkpoint kinase 2 (pCHK2). (ATR) Ataxia telangiectasia and Rad3-related, (ASO) antisense oligonucleotide. Vinculin was used as a control. (*F*) BLISS DSB count at transcription start/end sites (TSSs/TESs) (*top*) and region distribution (*bottom*). (Dashed line) Background (red box) promoter region. (*G*) Imaging (*left*) and quantitation (*right*) of phospho-Ser-139 histone H2A.X (γH2A.X) and Nibrin (NBS1) signals. (4-OHT) 4-hydroxytamoxifen, (white box) zoom. (*H,I*) ChIP for γH2A.X (*H*) and histone H2B lys-120 acetylation (H2BK120ac; *I*) at AsiSI site DS1. (noDSB) Control. (*) P-value < 0.05, (**) $P < 0.001$; two-tailed *t*-test or Wilcoxon test (BLISS). Error bar indicates mean ± SD or mean ± ±SEM (BLISS). (*n*) Number of cells.

NEAT1 chromatin occupancy and performed CHART-seq to assess NEAT1 occupancy at DSBs (Fig. 3A). We selectively enriched DNA from promoter-associated DSBs in the presence of 4-OHT but not upon STM2457 preincubation in DIvA cells (Fig. 3B). Reassuringly, NEAT1 was also enriched at promoters of highly expressed genes and at the originating *NEAT1* locus in unperturbed U2OS cells (Supplemental Fig. S4G,H). Visual inspection of browser tracks and manual CHART confirmed NEAT1 enrichment at DSBs (Fig. 3C; Supplemental Fig. S4I). To corroborate this, we combined RNA-FISH with antibody staining and observed modest NEAT1 colocalization with 53BP1-positive DSB foci upon etoposide treatment but not upon STM2457 preincubation (Supplemental Fig. S4J). To assess the proximity of NEAT1 to DSBs by an orthogonal assay, we used a recently published CRISPR/GFP-dCas13 system that allows GFP labeling of NEAT1 in vivo (Yang et al. 2019). We performed PLAs for GFP/γH2A.X and detected strong reactivity in etoposide-treated cells that expressed

NEAT1-selective guide RNA (Fig. 3D). We also performed RNA-PLAs, which report proximity between an antibody-stained protein and a DNA probe that hybridizes to a transcript of choice (Zhang et al. 2016). Again, we observed increased RNA-PLA signals in etoposide-treated cells upon combining an γH2A.X antibody with a NEAT1-selective antisense probe (Fig. 3E; Supplemental Fig. S4K). We conclude that NEAT1 accumulates at a minority fraction of DSBs in a METTL3-dependent manner.

DNA damage alters NEAT1 structure

m^{6}A marks can alter the structure and function of lncRNA (Liu et al. 2015). To assess whether DNA damage changes the structure of NEAT1, we applied in vivo RNA structural probing by dimethyl sulfate mutational profiling combined with nanopore sequencing (nano-DMS-MaP) (Zubradt et al. 2017; Bohn et al. 2023). Nano-DMS-MaP relies on methylation of unpaired adenines and

Figure 3. NEAT1 accumulates at promoter-associated DSBs in U2OS cells. (*A*) Scheme of CHART assay. (BIO) Biotin, (green) nucleosomes. (*B*,*C*) Heat map (*B*) and browser tracks (*C*) for NEAT1 CHART-seq read counts. (COs) Capturing oligonucleotides, (red box) quantified region of interest, (arrowhead) transcription start site. (*D*) Scheme of CRISPR-based NEAT1-labeling (*top*) and imaging of GFP (*bottom left*) and PLA (*bottom right*) signals. (Dashed line) Background. (*E*) Imaging (*top*) and quantitation (*bottom*) of RNA-PLA signals. (Dashed white circle) Nucleus, (dashed line) background. (*) *P*-value < 0.05, (**) *P* < 0.001; two-tailed *t*-test. Error bar indicates mean ± SD. (*n*) Number of replicates or cells.

cytosines, which creates mappable nucleotide exchanges upon reverse transcription (Supplemental Fig. S5A). We performed nano-DMS-MaP on two HEK293 cDNA amplicons to cover the entire NEAT1 isoform-overlapping sequence with high correlation among replicates (Supplemental Fig. S5B–D). As expected, DMS selectively modified adenines and cytosines irrespective of drug treatments (Supplemental Fig. S5E). Computational analysis of NEAT1 amplicon B predicted an ∼0.5 kb long secondary structure close to the etoposide-responsive METTL3 binding regions A and B that was selectively refolded by etoposide but not STM2457 preincubation (Fig. 4, refolding domain shaded in purple). Analysis of amplicon A revealed no significant response to etoposide treatment (data not shown). We conclude that NEAT1 refolds upon DNA damage in a METTL3-dependent manner.

NEAT1 sequesters CHD4 for release upon DNA damage

We hypothesized that NEAT1 refolding modulates its interactome and harnessed in situ proximity labeling data for NEAT1 in its native compartment (Yap et al. 2022). This approach identified 139 candidates (Fig. 5A). The chromodomain helicase DNA binding protein 4 (CHD4) histone deacetylase caught our attention, as it both promotes DSBR and binds several lncRNAs, including NEAT1 (Polo et al. 2010; Hendrickson et al. 2016; Zhao et al. 2018). To validate the interaction, we introduced an array of 24 RNA stem–loop-forming, capsid protein MS2 binding sites (MS2 tag) at the NEAT1 locus, which allowed immunoselection of MS2-NEAT1 upon expression of GFP-tagged MS2 coat protein. We confirmed the association of MS2-NEAT1 with both CHD4 and bona fide interactors of NEAT1 (SFPQ and NONO) in HEK293:24 × MS2-NEAT1 cells (Fig. 5B; Supplemental Fig. S6A–C). To corroborate this, we incubated radiolabeled in vitro transcribed NEAT1 with immunoselected endogenous CHD4 and observed strong, benzonase-sensitive enrichment of NEAT1 upon CHD4 pull-down (Fig. 5C). Prolonged exposure revealed the accumulation of a truncated NEAT1 fragment upon benzonase nuclease treatment, suggesting that CHD4 protected NEAT1 from complete endonucleolytic degradation. Next, we incubated equal amounts of HEK293 lysates containing GFP-tagged CHD4 (CHD4-GFP) or a GFP-tagged mouse double-minute 2 homolog (MDM2-GFP) control with in vitro transcribed, biotinylated, and bead-immobilized NEAT1 or control transcripts. Again, we observed prominent enrichment of CHD4-GFP but not MDM2-GFP upon pull-down with the NEAT1 in vitro transcription product (Fig. 5D; Supplemental Fig. S6D). As the N terminus of CHD4 confers RNA binding (Ullah et al. 2022), we repeated the pull-down assay with an N-terminal deletion mutant (ΔN-CHD4-GFP) and observed an approximately twofold weaker enrichment of ΔN-CHD4-GFP compared with CHD4-GFP (Supplemental Fig. S6E–G). To test whether CHD4 binding to NEAT1 is altered by DNA damage in vivo, we repeated the MS2-NEAT1 IP upon etoposide treatment, which impaired CHD4 association with MS2-NEAT1 (Supplemental Fig. S6H). RT-qPCR con-

firmed that etoposide treatment reduced the level of NEAT1 that coimmunoprecipitates with CHD4 approximately twofold (Fig. 5E). We also performed sucrose gradients and observed an etoposide-responsive decrease of CHD4 migration in higher-molecular-weight fractions that was suppressed by STM2457 and accompanied by decreased NEAT1 levels in those fractions (Fig. 5F,G). Importantly, RNase digestion shifted the positive control Nucleophosmin to lower fractions (Supplemental Fig. S6I). Moreover, seCLIP-seq revealed that CHD4 binds NEAT1 but not the DNA damage-inducible LINC01021 transcript (Fig. 5H; Supplemental Fig. S6J). CHD4 binding to both the NEAT1 isoform-overlapping sequence and the 3′ end of NEAT1_2 was sensitive to etoposide treatment. We conclude that DDR releases CHD4 from NEAT1.

Dysfunctional NEAT1 perturbs CHD4 occupancy, histone acetylation, and BRCA1 levels at DSBs

Our data suggest a METTL3–NEAT1–CHD4 signaling axis in DDR. Thus, we asked whether defects in METTL3 or NEAT1 perturb CHD4 occupancy at DSBs. We performed PLAs for CHD4/γH2A.X and detected prominent signals in 4-OHT-treated DIvA cells, which were partially sensitive to STM2457 (Supplemental Fig. S7A). CUT&RUN-seq confirmed that CHD4 occupancy was sensitive to STM2457 at the bulk of AsiSI-induced DSBs and particularly at nonpromoter DSBs that display low NEAT1 occupancy in our CHART-seq data. In contrast, CHD4 accumulated at NEAT1-positive, promoter-associated DSBs upon STM2457 preincubation (Fig. 6A; Supplemental Fig. S7B,C). Next, we assessed CHD4 occupancy in NEAT1-deficient cells. NEAT1 depletion did not alter CHD4 occupancy at the bulk of DSBs but mimicked STM2457 treatment at promoter-associated DSBs (Fig. 6B; Supplemental Fig. S7D,E). ChIP data for CHD4 confirmed elevated levels of CHD4 at the AsiSI site DS1 upon depletion of NEAT1 or STM2457 preincubation (Fig. 6C; Supplemental Fig. 7F), suggesting aberrant regulation of CHD4 by dysfunctional NEAT1. CHD4 mediates homologous recombination (HR) in cross-talk with the promoter mark histone H3 lys-27 acetylation (H3K27ac) and the breast cancer type 1 susceptibility protein (BRCA1) (Larsen et al. 2010; Smeenk et al. 2010; Reynolds et al. 2012). As dysfunctional NEAT1 shifts and elevates CHD4 occupancy ∼300 nt upstream of promoter-associated DSBs, we asked whether high CHD4 occupancy at DSBs in NEAT1-deficient cells correlates with defects in promoter-associated histone marks and BRCA1 recruitment. We assessed the levels of H3K27ac, histone H3 lys-4 trimethylation (H3K4me3), and BRCA1 at DS1 by ChIP (Fig. 6D,E; Supplemental Fig. S7G). Both histone marks but not BRCA1 were enriched at DS1 in unperturbed cells. However, H3K27ac was modestly reduced upon induction of DSBs by 4-OHT and strongly diminished in NEAT1-depleted, 4-OHT-treated DIvA cells. NEAT1 depletion also impaired the 4-OHT-induced recruitment of BRCA1 to DS1. Overall, we conclude that METTL3-dependent hypermethylation of NEAT1 releases and activates CHD4 to balance its chromatin
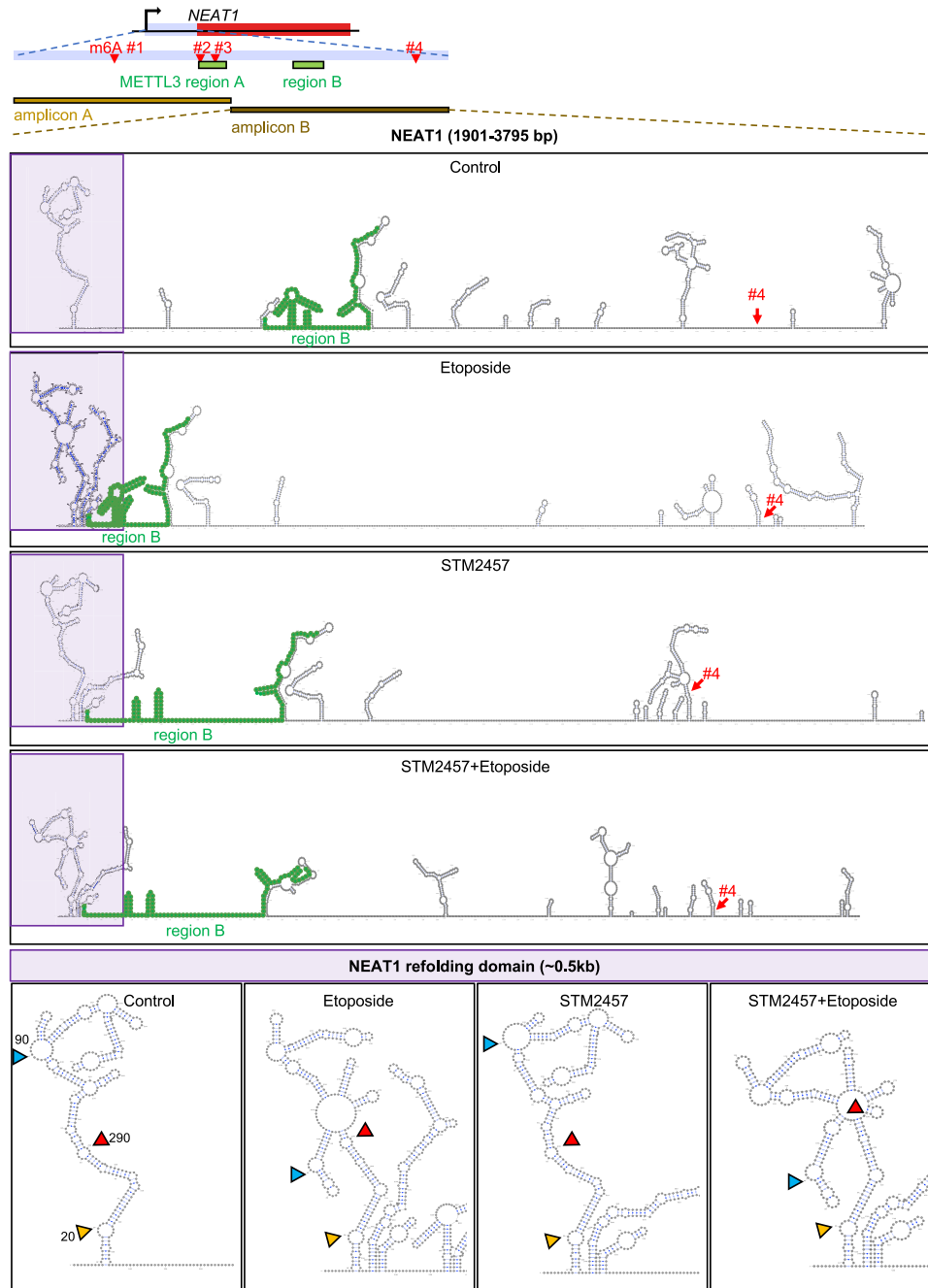
Figure 4. DNA damage alters NEAT1 structure in HEK293 cells. (*Top*) Scheme of m[6]A sites and METTL3 binding regions on NEAT1. (*Bottom*) Visualization of nano-DMS-MaP data from the NEAT1 isoform-overlapping amplicon B. (Green) METTL3 binding region B (triangle position marker).

occupancy and fine-tune H3K27ac levels at DS1 and other promoter-associated DSBs, which promotes BRCA1 recruitment and genome stability.

Discussion

We establish NEAT1 as novel regulator of DDR. NEAT1 modulates CHD4 function at promoter-associated DSBs

upon METTL3-dependent methylation, stabilization, and refolding (Fig. 6F). As the 1.8 kb NEAT1 isoform-overlapping region contains only one mapped m[6]A site, it seems likely that methylation of a single m[6]A site is not sufficient to induce NEAT1 refolding on a larger scale. The observed changes in NEAT1 secondary structure may be accompanied by methylation of additional m[6]A sites upstream of the NEAT1 refolding domain (in particular m[6]A sites 2 and 3). Alterations in the binding of
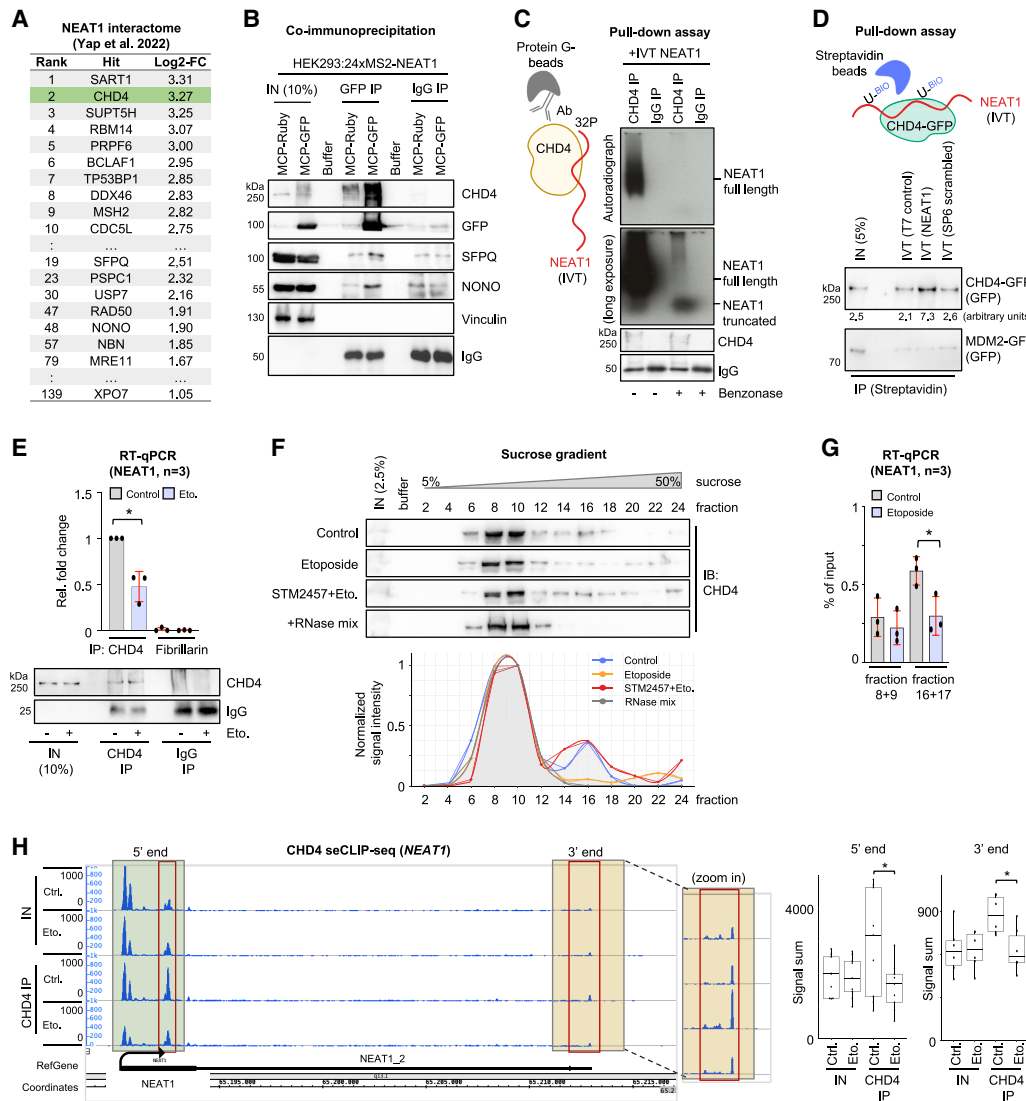
Figure 5. DNA damage impairs CHD4 association with NEAT1 in U2OS cells. (*A*) NEAT1 interactome analysis. (*B*) Immunoblots for chromodomain helicase DNA binding protein 4 (CHD4), GFP, SFPQ, and NONO in lysate (input [IN]) of GFP-tagged MS2 coat protein (MCP-GFP)-expressing HEK293:24×MS2-NEAT1 cells or upon IP with GFP antibody. IgG was used as a control. (*C*) Scheme of the pull-down assay (*left*) and an autoradiograph of 32P-γ-ATP end-labeled (32P) IVT product upon IP with immobilized CHD4 (*right*). IgG was used as a control, (Ab) antibody. (*D*) Scheme of the pull-down assay (*top*) and an immunoblot for GFP-tagged CHD4 (CHD4-GFP) in lysate (IN) or upon IP with biotin (BIO)-labeled IVT product (*bottom*). (IVT T7) IVT SP6 and mouse double-minute 2 homolog (MDM2), which were used as controls. (*E*) RT-qPCR assessing NEAT1 (*top*) and immunoblot (*bottom*) for CHD4 in lysate (IN) and upon IP. Fibrillarin and IgG were used as controls. (*F*) Immunoblot (IB) for CHD4 (*top*) and quantitation (*bottom*) in lysate (IN) or upon sucrose gradient fractionation. (*G*) RT-qPCR assessing NEAT1 from sucrose gradient fractions. (*H*) Browser tracks (*left*) and quantitation (*right*) of CHD4 seCLIP-seq reads. (Red box) Quantified region of interest (arrowhead) transcription start site.

METTL3 and other RBPs to NEAT1 or additional epitranscriptomic marks may also contribute to the phenotype. We acknowledge that although our analysis indicates DSB-induced structural changes in NEAT1, it does not pinpoint a distinct m^{6}A site with molecular switch-like function within NEAT1. The METTL3–NEAT1–CHD4 axis facilitates efficient DSBR likely in concert with chromatin breathing and additional factors (Smeenk and van Attikum 2013). However, downstream effectors of NEAT1-dependent DDR remain largely elusive. Does CHD4 function in the context of nucleosome remodeling

and deacetylase (NuRD) complexes? Although most NuRD complex components display RNA-binding properties, the in situ NEAT1 interactome contains only CHD4 and CHD3, which form distinct NuRD complexes with overlapping functionality in unperturbed cells (Hoffmeister et al. 2017; Caudron-Herger et al. 2019; Yap et al. 2022). Thus, distinct NuRD complexes likely occur also during DSBR. Besides NEAT1, CHD4 binds several other lncRNA and pre-mRNA transcripts, and the latter shield CHD4 from chromatin (Zhao et al. 2018; Ullah et al. 2022). As the METTL3 inhibitor STM2457, but not
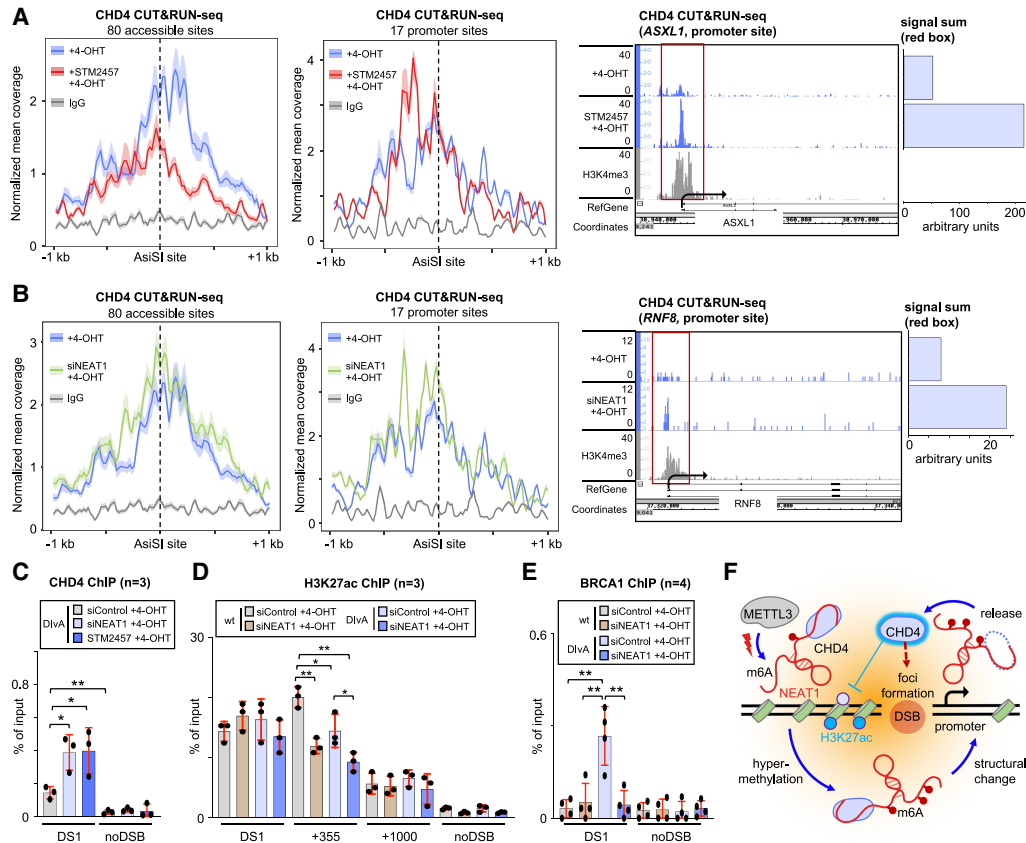
Figure 6. NEAT1 depletion deregulates CHD4 occupancy, histone acetylation, and BRCA1 levels at promoter-associated DSBs in U2OS cells. (*A,B*) Metagene plots (*left*) and browser tracks (*right*) of CHD4 CUT&RUN-seq data at AsiSI sites (dashed line) upon 4-OHT treatment and STM2457 preincubation (*A*) or NEAT1 depletion (*B*). (Red box) Quantified region of interest, (arrowhead) transcription start site. The +4-OHT condition is used as benchmark in both *A* and *B*. (*C–E*) ChIP for CHD4 (*C*), histone H3 lys-27 acetylation (H3K27ac) (*D*), or breast cancer type 1 susceptibility protein BRCA1 (*E*) at the AsiSI site DS1. (noDSB) Control. (*F*) Model illustrating our findings. See the text for details. (*) P-value < 0.05, (**) $P < 0.001$; two-tailed t-test. Error bar indicates mean ± SD. (*n*) Number of replicates.

NEAT1 depletion, diminished CHD4 occupancy at non-promoter DSBs, methylation of other transcripts may release CHD4 from ribonucleoprotein complexes to redundantly stimulate chromatin occupancy. METTL3 promiscuously modifies RNA, which includes methylation of nascent pre-mRNA and suppression of DNA–RNA hybrids (R-loops) at DSBs (Zhang et al. 2020; Raj et al. 2022). As a distinct NuRD complex drives R-loop-dependent histone deacetylation and chromatin remodeling of promoter-associated DSBs without CHD4 (Liu et al. 2024), methylation of both NEAT1 and R-loops may stimulate CHD4 occupancy.

NEAT1 depletion reduces the expression of DDR factors and induces γH2A.X (Taiana et al. 2020). Our contrary observation that NEAT1 depletion impairs DSB signaling may partially be explained by differences in the cellular system or variations in NEAT1 expression. Our data indicate that NEAT1 promotes DSB signaling upstream of γH2A.X. Why do DSB foci not form efficiently in NEAT1-deficient cells? First, the expression of factors that amplify DSB signaling may be compromised upon NEAT1 depletion (Mello et al. 2017). We did not observe severe cell cycle alterations upon NEAT1 depletion or ob-

vious impact on METTL3 or CHD4 levels. However, it remains to be determined to what extent other NEAT1-regulated RNA processes like miRNA biogenesis modulate our phenotype (Jiang et al. 2017). Second, NEAT1 may comprise an intrinsic property to promote DSB condensation. Arguing for the latter, phase-separating domains of NEAT1 have been identified that promote the formation of paraspeckles (Yamazaki et al. 2018). 53BP1 requires lncRNA for efficient recruitment to DSBs, and persistent AsiSI-induced DSBs cluster in distinct phase-separated structures (Pessina et al. 2019; Arnould et al. 2023). Thus, NEAT1 may be hijacked by DDR to catalyze condensation of DSBs.

We noticed that NEAT1 associates with a minor fraction of DSBs. Is NEAT1 DSB occupancy locus-selective? AsiSI sites are cleaved with different efficacies, depending on epigenetic modifications and chromatin accessibility. Promoter-associated DSBs often occur in actively transcribed regions and are prone to HR (Aymard et al. 2014). Thus, one possibility is that NEAT1 interactors modulate the access to DSBs; for instance, via association with the transcriptional machinery (Lewis et al. 2023). Our data do not unambiguously allocate the genome-

protective function of NEAT1 to a distinct isoform. This is partially due to technical constraints, limited assay sensitivities, and hindered probe accessibility to this structural lncRNA (West et al. 2014). We postulate that NEAT1_2 promotes genome stability. NEAT1_1 is not induced by etoposide and does not accumulate upon NEAT1_2 depletion. NEAT1_1 is indeed lowly expressed in proliferating cancer cells and is seemingly dispensable for homeostasis (Adriaens et al. 2016). Given that NEAT1 is deregulated in many tumors, the exploitation of the genome-protective role of NEAT1_2 may pave the way for novel RNA-centric therapeutics.

Materials and methods

Tissue culture, transfection, cloning, and viral work

Human U2OS, AsiSI-ER-expressing U2OS (DIvA; a kind gift from Gaelle Legube), HEK293, and HEK293:24 × MS2-NEAT1 cells were cultured in DMEM (Gibco) with 10% fetal bovine serum (FBS; Capricorn), 100 U/mL penicillin–streptomycin (Gibco), and 2 mM L-glutamine (Gibco) at 37°C and 5% CO_2 and periodically monitored for mycoplasma contamination. Drugs used were 20 µM etoposide (Sigma,) for 2 h, 10 µM 4-hydroxytamoxifen (4-OHT; Sigma) for 4 h, 1 µM ATM inhibitor KU-55933 (Hycultec) for 2 h, or 10 µM METTL3 inhibitor STM2457 (Hycultec) for 16 h, or stated differently. For sorting, cells were washed and resuspended in 1 mL of PBS, fixed for 16 h at −20°C in 4 mL of 100% ethanol, centrifuged at 1500 rpm for 10 min, washed in PBS, repelleted, resuspended to $1 × 10^6$ cells/mL in 1 mL of PBS, stained for 30 min at 37°C in the dark with 54 µM propidium iodide and 24 µg/mL RNase A (Sigma), sorted (FACSDiva 9.0.1, BD Biosciences), and analyzed. Small interfering (si) RNA, antisense oligonucleotides (ASOs) or plasmids (Supplemental Tables S1–S3) were transfected with Lipofectamine2000 (Invitrogen) and Opti-MEM (Gibco) following the manufacturer's protocol. The CHD4 mutant was cloned with primers (Supplemental Table S4) and a Q5 site-directed mutagenesis kit (NEB) following the manufacturer's protocol. The pCRII-TOPO-NEAT1_1 template (a kind gift from Archa Fox) was digested with BamHI/NcoI (NEB), PCR-amplified with Phusion polymerase (NEB) and primers (Supplemental Table S4), redigested with BamHI or NotI (both from NEB), and purified (PCR clean-up kit, NEB) following the manufacturer's protocols. To produce virus, 10 µg of pHAGE-IRES-puro-NLS-dPspCas13b-EGFP-3xFLAG (a kind gift from Ling Ling Chen), 10 µg of pPAX2 (a kind gift from Elmar Wolf), and 2.5 µg of pMD2.G (a kind gift from Elmar Wolf) plasmids were mixed with 30 µL of polyethylenimine (Calbiochem); diluted in 500 µL of OptiMEM; vortexed; incubated for 25 min at room temperature; added dropwise to HEK293 cells; and incubated for 8 h. Viral supernatant was harvested every 12 h three times, filtered, and frozen at −80°C. For polyclonal selection of U2OS:dPspCas13-GFP cells, parental cells were cultured for 24 h with 1.5 mL of DMEM, 1.5 mL of supernatant,

6 µL of polybrene (Invitrogen), and 2 µg/mL puromycin (Invivogen) for 10 days. Validated single-guide (sg)RNA (g3′-2-v3) was used for targeting of NEAT1 (Yang et al. 2019). Carrying vector pC0043-dPspCas13b-sgRNA was created from pC0043-dPspCas13b (Addgene) by digestion for 60 min at 37°C with BbsI (NEB), ligation for 30 min at 37°C with sgRNA-encoding duplex DNA (Supplemental Table S4) by T4 DNA ligase (NEB), and amplification in *Escherichia coli*. Plasmids were verified by sequencing. Monoclonal HEK293:24 × MS2-NEAT1 cells were obtained by transfection of HEK293 cells with 1.3 µg of bicistronic nuclease plasmid and 0.7 µg of MS2 knock-in donor plasmid (kind gifts from Ling Ling Chen) with TurboFect reagent (Thermo) as described (Yang et al. 2019). Puromycin-selected cells were sorted (BD FACSMelody, BD Biosciences), and knock-in was confirmed by PCR with DreamTaq DNA polymerase (Thermo) and junction primer pairs (Supplemental Table S4) following the manufacturer's protocol. Clones with correct PCR products were validated by agarose gel electrophoresis.

Immunoblotting and immunoprecipitation (IP)

Cells were lysed in sample buffer (250 mM Tris-HCl at pH 6.8, 8% SDS, 40% glycerol, 0.8% β-mercaptoethanol, 0.02% bromophenol blue), boiled for 5 min at 95°C, and sonicated. Whole-cell lysates were separated by SDS-PAGE, transferred to nitrocellulose membranes (Cytiva), stained with 0.5% Ponceau S/1% acetic acid, blocked, washed in PBS/0.1% Triton X-100/5% milk (PBST), probed with antibodies (Supplemental Table S5) or a streptavidin-HRP probe (Invitrogen), visualized with an ECL kit (Cytiva) on an imaging station (LAS-4000 Fuji or Fusion FX Vilber), and quantified by ImageJ (NIH) following the manufacturer's protocols. For IP, cells were lysed for 10 min at 4°C in 5 vol of IP buffer (200 mM NaCl, 0.5 mM EDTA, 20 mM HEPES, 0.2% NP-40, 10% glycerol, 100 U of RNase inhibitor [Ribolock; Thermo], 1× protease/phosphatase inhibitor [Roche]) and centrifuged at 12,000 rpm for 12 min. Supernatants were incubated for 2 h at 4°C with 2–5 µg of antibodies and preconjugated to 25 µL of protein G Dynabeads (Invitrogen). Complexes were immobilized on a magnet (Invitrogen), washed in 800 µL of IP buffer for 10 min at 4°C, and eluted in sample buffer.

Imaging

Cells were grown on coverslips (Roth), washed in PBS, fixed for 10 min in 3% paraformaldehyde (Sigma), washed in PBS, permeabilized with PBS/0.1% Triton X-100 for 10 min, and blocked with PBS/10% FBS for 2 h at 4°C. Antibodies (Supplemental Table S5) were diluted in PBS/0.15% FBS and incubated for 16 h at 4°C or for 2 h at room temperature. Cells were washed in PBS/0.1% Triton X-100, sealed in 6-diamidino-2-phenylindole (DAPI)-containing mounting medium (VectaShield), and imaged on CLSM-Leica-SP2 or CLSM-Leica--SP8 at 1024 × 1024 resolution (airy = 1). Channels were acquired

as single snapshots, sequentially, between frames, with equal exposure times (eight or more acquisitions). Colocalization was assessed by the Pearson correlation coefficient with JACoP (ImageJ). Proximity ligation assays (PLAs) were performed with a Duolink kit (Sigma) following the manufacturer's protocol. For RNA-PLAs, cells were washed, fixed, and permeabilized as above and incubated for 1 h at 4°C in RNA-PLA blocking buffer (10 mM Tris-HCl, at pH 7.5, 10 mM MgAc, 50 mM KAc, 250 mM NaCl, 0.25 µg/µL bovine serum albumin [BSA], 0.05% Triton X-100, 100 U of Ribolock). Cells were then incubated for 16 h at 4°C with RNA-PLA probes (Supplemental Table S6), which were prediluted to 100 nM in RNA-PLA blocking buffer and preheated for 3 min at 70°C. Samples were washed in PBS, incubated for 2 h at 4°C in PLA blocking solution (Sigma), washed in PBS, and incubated for 16 h at 4°C with appropriately diluted primary antibody. Subsequent steps were as above with MINUS probe only. RNA fluorescence in situ hybridization (RNA-FISH) experiments were performed following the manufacturer's protocol with a predesigned Quasar570- or Quasar670-labeled NEAT1 5′ segment or mid-domain probes (Stellaris SMF-2036-1 or VSMF-2251-5). For CRISPR/Cas13 labeling, U2OS:dPspCas13-GFP cells were lipofected with carrying vector pC0043-dPspCas13b-sgRNA, subjected to PLAs 24 h later, and imaged. For neutral comet assay, glass slides (Roth) were coated with 0.01% poly-L-lysine (Sigma) and 1% agarose (Roth) and incubated for 16 h at 70°C in a hybridization oven (UVP). Cells were washed in PBS, counted to 1×10^5 cells/mL, mixed 1:1 with PBS/1.5% low-melting agarose (Biozym), pipetted onto glass slides, and incubated for 10 min at 4°C. Samples were lysed for 1 h at 4°C in buffer A (2.5 M NaCl, 0.1 M EDTA, 0.1 M Tris-HCl at pH 10, 1% Triton X-100) without coverslips, covered with parafilm, washed in PBS, subjected to electrophoresis for 15 min at 4°C and 1 V/cm in buffer B (100 mM Tris at pH 8.5, 300 mM NaAc), fixed in 70% ethanol, dried for 16 h at room temperature, stained for 20 min in the dark in PBS/1× SYBR Gold (Thermo), imaged, and quantified with CometScore software.

RNA analytics

Total or immunoselected RNA was isolated with TRIzol (Invitrogen), and cDNA was synthesized with SuperScript III reverse transcriptase (Invitrogen) and selective primers (Supplemental Table S7), random hexamer primer (Thermo), or oligo-dT-18 primer (Thermo) and quantified upon reverse transcription by quantitative PCR (RT-qPCR) in a thermocycler (Applied) with PowerUp SYBR Green master mix (Applied) following the manufacturer's protocols. For dot blots, total RNA was resuspended in 0.02% methylene blue, heated for 5 min at 72°C, spotted on a nylon membrane (Cytiva), cross-linked at 254 nm and 120 mJ/cm² with UVP, blocked for 20 min at room temperature in PBS/0.1% Triton X-100/0.5% SDS, and subjected to immunoblotting. For immunoselection, 10 µg of total RNA was diluted in 800 µL of IP buffer, incubated for 2 h at 4°C with 10 µg of antibody,

and purified as above. For qualitative analysis, RNA was incubated for 10 min at 75°C in 1 vol of 2× urea dye (7 M urea, 0.05% xylene cyanol, 0.05% bromophenol blue), separated for 30 min at 350 V by 8 M urea-PAGE in TBE buffer (90 mM Tris, 90 mM boric acid, 2 mM EDTA), stained for 20 min in the dark with 1× SYBR Gold (Thermo), and visualized on a transilluminator (Thermo) or analyzed on a fragment analyzer (Agilent).

In vitro transcription (IVT), pull-downs, and S-adenosyl-methionine (SAM)fluoro assay

To synthesize nonmethylated or biotin-16-UTP-labeled NEAT1 in vitro, 1 µL of 500 ng/µL IVT template or control template (Jena Biosciences) was subjected to IVT for 4 h at 37°C using high-yield T7 biotin16 RNA labeling kit (Jena Biosciences) according to the manufacturer's protocol. The scrambled control was transcribed with a SP6 transcription kit (Jena Biosciences) accordingly. To monitor integrity, RNA was resuspended in 2× RNA loading buffer (50% formamide, 15% formaldehyde, 40 mM MOPS, 10 mM NaAc, 1 mM EDTA at pH 7.0, 0.1% bromophenol blue, 10 µg/mL ethidium bromide) and separated for 90 min at 100 V on a 1.2% agarose gel with 5.5% paraformaldehyde and 1× MOPS buffer (40 mM MOPS, 10 mM NaAc, 1 mM EDTA at pH 7.0). For pull-downs, IVT product was incubated for 1 h at 37°C with labeling mix (1 µL of 10× PNK buffer [NEB], 1 µL of IVT product, 1 µL of T4 PNK [NEB], 1 µL of γ-^{32}P-ATP [Hartmann], 1 µL of 100 U of Ribolock 5 µL of ddH$_2$O) and centrifuged at 3200 rpm for 5 min with G-25 columns (Cytiva). The labeled IVT product was diluted in 800 µL of IP buffer, incubated with rotation for 2 h at room temperature with immunoselected CHD4, washed in 800 µL of IP buffer, and again incubated for 5 min at room temperature with 10 U of benzonase (Millipore) or buffer. The RNA was purified with TRIzol, separated on a 1.2% agarose gel, and visualized by autoradiography with hyperfilms (Cytiva). One microgram of biotin-16-UTP-labeled NEAT1 was immobilized on 25 µL of streptavidin C1 Dynabeads (Invitrogen), washed in 800 µL of IP buffer, and incubated with rotation for 2 h at room temperature with immunoselected FLAG-METTL3 or CHD4-GFP variants. Complexes were captured on a magnet, washed in 800 µL of IP buffer, eluted for 5 min at 95°C in sample buffer, and analyzed by immunoblotting. For SAMfluoro assay, immunoselected FLAG-METTL3 variants were resuspended in 250 µL of assay buffer (G-Biosciences), mixed with 50 µL of ddH$_2$O containing 1 µg of nonmethylated IVT product, aliquoted to 100 µL in 96 well plates containing 100 µL of reaction mix (G-Biosciences) per well, and measured on a TECAN plate reader according to the manufacturer's protocols.

Subcellular fractionation

Cells were lysed for 10 min at 4°C in 5 vol of CP buffer (10 mM HEPES at pH 7.9, 60 mM KCl, 1.5 mM MgCl$_2$, 1 mM EDTA, 1 mM DTT, 0.075% NP-40, 1× protease/phosphatase inhibitor) and centrifuged at 1200 rpm for 10 min at 4°C. The soluble lysate was recentrifuged at 13,500 rpm for

10 min at 4°C, and supernatant was collected as cytoplasmic fraction. Pelleted nuclei were washed in 800 µL of CP buffer without NP-40, lysed for 10 min at 4°C in 1 vol of NP buffer (20 mM HEPES at pH 7.9, 400 mM NaCl, 1.5 mM MgCl$_2$, 0.2 mM EDTA, 1 mM DTT, 5% glycerol, 1× protease/phosphatase inhibitor), and centrifuged at 13,500 rpm for 10 min at 4°C. The nuclear lysate was diluted in 2 vol of DIL buffer (20 mM HEPES at pH 7.9, 1.6% Triton X-100, 0.2% sodium deoxycholate [DOC], 1× protease/phosphatase inhibitor), sonified (Branson), incubated for 5 min at room temperature with 10 U of benzonase (Sigma), and centrifuged at 13,500 rpm for 10 min at 4°C. Supernatant was collected as nuclear fraction.

Sucrose gradients

Sucrose (5% or 50%) in 10 mM Tris-HCl (pH 7.5), 1 mM EDTA, and 100 mM NaCl was layered in ultracentrifuge tubes (Beckman) and mixed by gradient maker (Biocomp). Cells were lysed for 30 min at 4°C in 100 µL of lysis buffer (25 mM Tris-HCl at pH 7.4, 105 mM KCl, 0.5% NP-40, 2 mM EDTA, 1 mM NaF, 0.5 mM DTT, 100 U of Ribolock, 1× protease/phosphatase inhibitor), homogenized with a syringe (BD Microlane #14), and centrifuged at 13,000 rpm for 10 min at 4°C. Supernatant was loaded on the gradient and centrifuged (Beckman) at 30,000 rpm for 18 h at 4°C or kept as input (5%). Fractions were precipitated for 10 min at room temperature with 50 µL of 0.15% DOC and 25 µL of 100% trichloroacetic acid, incubated for 30 min at 4°C, centrifuged at 12,000 rpm for 15 min at 4°C, washed in 500 µL of acetone, recentrifuged, air-dried, and resuspended in sample buffer. RNA was digested for 1 h at 4°C with a mix of 2.5 µL of 10 mg/mL RNase A, 2.5 µL of 10 U/µL RNase I, 2.5 µL of 1000 U/µL RNase T1, 2.5 µL of 5 U/µL RNase H, and 2.5 µL of 1 U/µL RNase III (all Thermo).

Chromatin immunoprecipitation (ChIP) and CUT&RUN sequencing

For ChIP, cells were fixed with 1% formaldehyde for 10 min at 37°C, quenched in 0.125 M glycine for 10 min at 37°C, washed in PBS, and centrifuged at 2000 rpm for 5 min. Pellets were lysed for 10 min at 4°C in 500 µL of buffer I (5 mM PIPES at pH 8.0, 85 mM KCl, 0.5% NP-40, 1× protease/phosphatase inhibitor). Nuclei were centrifuged at 3000 rpm at 5 min, and pellets were lysed for 10 min at 4°C in 300 µL of buffer II (1% SDS, 10 mM EDTA, 50 mM Tris-HCl at pH 8.0, 1× protease/phosphatase inhibitor). Lysate was sonicated five times for 5 min with 30 sec on/off with a Bioruptor (Diagenode) and pelleted at 13,000 rpm for 10 min. Supernatant was mixed with 2 mL of dilution buffer (0.01% SDS, 1.1% Triton X-100, 1.2 mM EDTA, 16.7 mM Tris-HCl at pH 8.0, 167 mM NaCl, 1× protease/phosphatase inhibitor). Diluted samples were aliquoted, and 5 µg of antibodies was added (IP sample) or not (input) and incubated with rotation for 16 h at 4°C. For pull-down, 20 µL of protein G Dynabeads was added to IP samples, incubated with rotation for 1 h, immobilized on a magnet, and washed once each in buff-

ers A (0.1% SDS, 1% Triton X-100, 2 mM EDTA, 20 mM Tris-HCl at pH 8.0, 150 mM NaCl), B (0.1% SDS, 1% Triton X-100, 2 mM EDTA, 20 mM Tris-HCl at pH 8.0, 500 mM NaCl), and C (0.25 M LiCl, 1% NP-40, 1% DOC, 1 mM EDTA, 10 mM Tris-HCl at pH 8.0) and twice in buffer D (10 mM Tris-HCl at pH 8.0, 1 mM EDTA). Samples were incubated for 30 min at room temperature with 500 µL of elution buffer (1% SDS, 0.1 M NaHCO$_3$), and cross-links were reversed overnight at 65°C with 30 µL of 5 M NaCl, 1 µL of 10 mg/mL RNase A, 10 µL of 0.5 M EDTA, 20 µL of 1 M Tris-HCl (pH 6.8), and 2 µL of 10 mg/mL proteinase K (Sigma). DNA was purified by phenol/chloroform extraction and assessed by qPCR with primers (Supplemental Table S7). For CUT&RUN-seq, cells were harvested with accutase (Sigma), centrifuged at 2500 rpm for 3 min, washed in 1.5 mL of wash buffer (20 mM HEPES at pH 7.5, 150 mM NaCl, 0.5 mM spermidine), incubated for 10 min at room temperature with 10 µL of concanavalinA-coated magnetic beads (Bio-Mag), immobilized on a magnet, permeabilized with 150 µL of antibody buffer (20 mM HEPES at pH 7.5, 150 mM NaCl, 0.5 mM spermidine, 0.05% digitonin, 2 mM EDTA), and incubated with 1 µg of antibody for 16 h at 4°C with rotation. Samples were immobilized on a magnet, washed in 1 mL of dig-wash buffer (20 mM HEPES at pH 7.5, 150 mM NaCl, 0.5 mM spermidine, 0.05% digitonin), incubated with rotation for 1 h at 4°C with 150 µL of 1 µg/mL protein A/G–micrococcal nuclease fusion (Cell Signaling Technology), immobilized, washed in 1 mL of rinse buffer (20 mM HEPES at pH 7.5, 0.05% digitonin, 0.5 mM spermidine), and incubated for 30 min at 4°C in digestion buffer (3.5 mM HEPES at pH 7.5, 10 mM CaCl$_2$, 0.05% digitonin). The reaction was quenched with 200 µL of stop buffer (170 mM NaCl, 20 mM EGTA, 0.05% digitonin, 50 µg/mL RNase A, 25 µg/mL glycogen), and fragments were released by incubation for 30 min at 37°C. Supernatant was incubated for 1 h at 50°C with 2 µL of 10% SDS and 5 µL of 10 mg/mL proteinase K (Sigma). Chromatin was recovered by phenol/chloroform extraction and resuspended in 30 µL of TE (1 mM Tris-HCl at pH 8.0, 0.1 mM EDTA). For sequencing, three biological replicates were quantified by fragment analyzer, pooled, and subjected to library preparation. Libraries for small DNA fragments (25–75 bp) were prepared with NEBNext Ultra II DNA library preparation kit for Illumina (NEB).

Capture hybridization analysis of RNA targets (CHART) and CHART-seq

Cells were cross-linked, lysed, and sonicated as above. Supernatant was diluted in 1 mL of capturing buffer (0.5 M LiCl, 4 M urea, 100 U of Ribolock, 1× protease/phosphatase inhibitor) containing 100 nM biotin-tagged capturing oligonucleotides (Supplemental Table S8) or not and incubated with shaking for 3 h at 65°C or kept as input (10%). Samples were incubated with rotation for 45 min at room temperature with 30 µL of streptavidin C1 Dynabeads (Thermo), immobilized, washed with 800 µL of capturing buffer, and eluted for 30 min at room temperature in 500

µL of elution buffer (1% SDS, 0.1 M NaHCO$_3$). Reversal of cross-links, phenol/chloroform extraction, and quantitation by qPCR were as above. For CHART-seq, three biological replicates were pooled and subjected to library preparation with NEBNext Ultra II DNA library preparation kit for Illumina (NEB).

Break labeling in situ and sequencing (BLISS)

Cells were washed in PBS, fixed for 10 min at room temperature with 5% formaldehyde, washed in PBS, lysed for 1 h at 4°C in buffer 1 (10 mM Tris-HCl at pH 8.0, 10 mM NaCl, 1 mM EDTA, 0.2% Triton X-100), washed in PBS, lysed for 1 h at 37°C in buffer 2 (10 mM Tris-HCl at pH 8.0, 150 mM NaCl, 1 mM EDTA, 0.3% SDS), and washed in PBS. For restriction, samples were equilibrated for 2 min at room temperature in 150 µL of 1× Cut-Smart (CS) buffer (NEB) and incubated for 2 h at 37°C with 10 U/µL AsiSI endonuclease (NEB) or buffer. For blunting, samples were washed in 1× CS buffer and incubated for 1 h at room temperature in 150 µL of reaction mix (112.5 µL of ddH$_2$O, 15 µL of 10× blunting buffer [NEB], 15 µL of 100 µM dNTPs, 0.3 µL of 50 mg/mL BSA, 6 µL of blunting enzyme mix from quick blunting kit [NEB]). Samples were washed in 1× CS buffer and 1× T4 ligase buffer (NEB), ligated for 18 h at 16°C in 150 µL of LIG buffer (124.5 µL of ddH$_2$O, 15 µL of 10× T4 ligase buffer, 3 µL of 50 mg/mL BSA, 1.5 µL of 2000 U/µL T4 ligase [NEB], 6 µL of BLISS preannealed adapters) (Supplemental Table S9), and washed for 1 h at 37°C in HSW buffer (10 mM Tris-HCl at pH 8.0, 2 M NaCl, 2 mM EDTA, 0.5% Triton X-100). DNA was incubated for 18 h at 55°C in 100 µL of extraction buffer (10 mM Tris-HCl at pH 8.0, 100 mM NaCl, 50 mM EDTA, 1% SDS, 10 mg/mL 10% proteinase K), harvested by scraping, pooled, purified by phenol/chloroform extraction, recovered in ddH$_2$O, sonicated (Covaris), concentrated on a magnet with SPRI select beads (Beckman), washed in 80% ethanol, air-dried, and eluted in ddH$_2$O. For IVT, 7.5 µL of DNA was incubated for 14 h at 37°C with IVT mix (0.5 µL of Ribolock, 2 µL of T7 polymerase buffer [NEB], 8 µL of rNTP mix, 2 µL of T7 polymerase [Invitrogen]). IVT product was incubated for 15 min with 5 µL of Turbo DNase (Invitrogen), size-selected with RNAClean XP beads (Beckman), washed in 80% ethanol, eluted in ddH$_2$O, and subjected to library preparation as above. Data analysis was as described (Trifault et al. 2024). Reads were demultiplexed based on barcodes with UMI-tools and mapped with Bowtie2. Samples were filtered against an ENCODE Blacklist to remove high variance in mappability with BEDtools intersect. Duplicated reads were identified via UMI, grouped, and deduplicated with UMI-tools. Two biological replicates were merged prior to mapping and collectively processed. The bar graph was generated with R package exomeCopy 3 kb upstream of and downstream from the TSS and divided by the number of genes. U2OS RNA-seq data were filtered by gene length (≥1500 bp) and used to stratify highly and lowly expressed genes. Distribution was generated with R package ChIPseeker.

Generation of NGS files, metagene plots, heat maps, bar charts, and schemes

Base calling was performed with FASTQ generation software (Illumina). Reads were mapped with Bowtie2 (Langmead and Salzberg 2012) to hg19, T2T, or mm10. Samples were read-normalized, and normalized BAM files were sorted and indexed with SAMtools. Bedgraph files were generated with BEDtools genomecov from the BEDTools suite (Quinlan and Hall 2010). Metagene plots were generated with the R package metagene. Reads were counted with BEDTools. Data were visualized with RStudio (ggplot2), Integrated Genome Browser, or Prism (GraphPad). 4sU-seq data were obtained from a previously published work (Trifault et al. 2024). Schemes were created with BioRender.

Single-end enhanced cross-linking immunoprecipitation (seCLIP) sequencing

Cells were washed in PBS, aspirated, cross-linked at 254 nm and 400 mJ/cm^2 with UVP, resuspended in PBS, scraped, centrifuged at 1200 rpm for 5 min, incubated for 5 min at 4°C in 1 mL of lysis buffer (50 mM Tris-HCl at pH 7.4, 100 mM NaCl, 1% NP-40, 0.1% SDS, 0.5% DOC, 440 U of RNase inhibitor [Thermo], 1× protease/phosphatase inhibitor), sonicated, digested for 5 min at 37°C with 40 U of RNase I (Invitrogen) and 10 U of Turbo DNase, and centrifuged at 13,000 rpm for 10 min. Supernatant was incubated with rotation for 16 h at 4°C with 15 µg of antibodies, which were preconjugated to 63 µL of protein A/G Dynabeads (Invitrogen). Immunocomplexes were captured on a magnet and washed in 800 µL of buffer WB-I (50 mM Tris-HCl at pH 7.4, 1 M NaCl, 1% NP-40, 1 mM EDTA, 0.1% SDS, 0.5% DOC) and 800 µL of buffer WB-II (20 mM Tris-HCl at pH 7.4, 10 mM MgCl$_2$, 0.2% Tween-20, 5 mM NaCl). Sequencing libraries and data analysis were as described (Van Nostrand et al. 2016; Blue et al. 2022). Adapters were trimmed with Cutadapt (v1.14). Trimmed FASTQ files were aligned to a genome index consisting only of Repbase annotated repetitive elements with STAR aligner (v2.7.6a). Repetitive elements were excluded. Mapped BAM files were sorted with SAMtools, and duplicates were removed by a custom Python script (Blue et al. 2022). Read-normalized BAM files were converted to bigwig files with deeptools (v3.5.1) bamCoverage. Bigwig files and log$_2$ fold changes of two biological replicates were merged by calculating averages with deeptools bigwigCompare. For box plots, regions of interests were split into bins of the same length, and signal sum was calculated as log$_2$ fold change.

Dimethyl sulfate mutational profiling with nanopore sequencing (nano-DMS-MaP)

Cells were incubated for 6 min at 37°C with 25 mM DMS, washed in PBS/1% β-mercaptoethanol, scraped, and centrifuged at 1200 rpm for 5 min. Ten micrograms of TRIzol-extracted total RNA was digested for 5 min at 37°C

with 10 U of Turbo DNase, column-purified (NucleoSpin, Macherey Nagel), reverse-transcribed to cDNA, amplified with primers (Supplemental Table S10), and assessed by fragment analyzer. Library preparation of two biological replicates and analysis was as described (Bohn et al. 2023).

Data availability

Sequencing data are available at Gene Expression Omnibus (CHART-seq: GSE255340, seCLIP-seq: GSE255341, CUT& RUN-seq: GSE255342, nano-DMS-MaP: GSE256233, and BLISS: GSE273351). Requests for resources and reagents should be directed to the corresponding author.

References

Adriaens C, Standaert L, Barra J, Latil M, Verfaillie A, Kalev P, Boeckx B, Wijnhoven PW, Radaelli E, Vermi W, et al. 2016. p53 induces formation of NEAT1 lncRNA-containing paraspeckles that modulate replication stress response and chemosensitivity. *Nat Med* **22:** 861–868. doi:10.1038/nm.4135

Arnould C, Rocher V, Saur F, Bader AS, Muzzopappa F, Collins S, Lesage E, Le Bozec B, Puget N, Clouaire T, et al. 2023. Chromatin compartmentalization regulates the response to DNA damage. *Nature* **623:** 183–192. doi:10.1038/s41586-023-06635-y

Aymard F, Bugler B, Schmidt CK, Guillou E, Caron P, Briois S, Iacovoni JS, Daburon V, Miller KM, Jackson SP, et al. 2014. Transcriptionally active chromatin recruits homologous recombination at DNA double-strand breaks. *Nat Struct Mol Biol* **21:** 366–374. doi:10.1038/nsmb.2796

Blackford AN, Jackson SP. 2017. ATM, ATR, and DNA-PK: the trinity at the heart of the DNA damage response. *Mol Cell* **66:** 801–817. doi:10.1016/j.molcel.2017.05.015

Blue SM, Yee BA, Pratt GA, Mueller JR, Park SS, Shishkin AA, Starner AC, Van Nostrand EL, Yeo GW. 2022. Transcrip-

tome-wide identification of RNA-binding protein binding sites using seCLIP-seq. *Nat Protoc* **17:** 1223–1265. doi:10.1038/s41596-022-00680-z

Bohn P, Gribling-Burrer AS, Ambi UB, Smyth RP. 2023. Nano-DMS-MaP allows isoform-specific RNA structure determination. *Nat Methods* **20:** 849–859. doi:10.1038/s41592-023-01862-7

Burger K, Schlackow M, Potts M, Hester S, Mohammed S, Gullerova M. 2017. Nuclear phosphorylated dicer processes doublestranded RNA in response to DNA damage. *J Cell Biol* **216:** 2373–2389. doi:10.1083/jcb.201612131

Burger K, Ketley RF, Gullerova M. 2019a. Beyond the Trinity of ATM, ATR, and DNA-PK: multiple kinases shape the DNA damage response in concert with RNA metabolism. *Front Mol Biosci* **6:** 61. doi:10.3389/fmolb.2019.00061

Burger K, Schlackow M, Gullerova M. 2019b. Tyrosine kinase c-Abl couples RNA polymerase II transcription to DNA doublestrand breaks. *Nucleic Acids Res* **47:** 3467–3484. doi:10.1093/nar/gkz024

Caron P, van der Linden J, van Attikum H. 2019. Bon voyage: a transcriptional journey around DNA breaks. *DNA Repair (Amst)* **82:** 102686. doi:10.1016/j.dnarep.2019.102686

Caudron-Herger M, Rusin SF, Adamo ME, Seiler J, Schmid VK, Barreau E, Kettenbach AN, Diederichs S. 2019. R-DeeP: proteome-wide and quantitative identification of RNA-dependent proteins by density gradient ultracentrifugation. *Mol Cell* **75:** 184–199.e10. doi:10.1016/j.molcel.2019.04.018

Chowdhury D, Choi YE, Brault ME. 2013. Charity begins at home: non-coding RNA functions in DNA repair. *Nat Rev Mol Cell Biol* **14:** 181–189. doi:10.1038/nrm3523

Ciccia A, Elledge SJ. 2010. The DNA damage response: making it safe to play with knives. *Mol Cell* **40:** 179–204. doi:10.1016/j.molcel.2010.09.019

Clouaire T, Rocher V, Lashgari A, Arnould C, Aguirrebengoa M, Biernacka A, Skrzypczak M, Aymard F, Fongang B, Dojer N, et al. 2018. Comprehensive mapping of histone modifications at DNA double-strand breaks deciphers repair pathway chromatin signatures. *Mol Cell* **72:** 250–262.e6. doi:10.1016/j.molcel.2018.08.020

Dutertre M, Lambert S, Carreira A, Amor-Guéret M, Vagner S. 2014. DNA damage: RNA-binding proteins protect from near and far. *Trends Biochem Sci* **39:** 141–149. doi:10.1016/j.tibs.2014.01.003

Fox AH, Nakagawa S, Hirose T, Bond CS. 2018. Paraspeckles: where long noncoding RNA meets phase separation. *Trends Biochem Sci* **43:** 124–135. doi:10.1016/j.tibs.2017.12.001

García-Muse T, Aguilera A. 2019. R loops: from physiological to pathological roles. *Cell* **179:** 604–618. doi:10.1016/j.cell.2019.08.055

Hendrickson DG, Kelley DR, Tenen D, Bernstein B, Rinn JL. 2016. Widespread RNA binding by chromatin-associated proteins. *Genome Biol* **17:** 28. doi:10.1186/s13059-016-0878-3

Hirose T, Ninomiya K, Nakagawa S, Yamazaki T. 2023. A guide to membraneless organelles and their various roles in gene regulation. *Nat Rev Mol Cell Biol* **24:** 288–304. doi:10.1038/s41580-022-00558-8

Hoffmeister H, Fuchs A, Erdel F, Pinz S, Gröbner-Ferreira R, Bruckmann A, Deutzmann R, Schwartz U, Maldonado R, Huber C, et al. 2017. CHD3 and CHD4 form distinct NuRD complexes with different yet overlapping functionality. *Nucleic Acids Res* **45:** 10534–10554. doi:10.1093/nar/gkx711

Jackson SP, Bartek J. 2009. The DNA-damage response in human biology and disease. *Nature* **461:** 1071–1078. doi:10.1038/nature08467

Jiang L, Shao C, Wu QJ, Chen G, Zhou J, Yang B, Li H, Gou LT, Zhang Y, Wang Y, et al. 2017. NEAT1 scaffolds RNA-binding proteins and the Microprocessor to globally enhance pri-miRNA processing. *Nat Struct Mol Biol* **24:** 816–824. doi:10.1038/nsmb.3455

Kastan MB, Lim DS. 2000. The many substrates and functions of ATM. *Nat Rev Mol Cell Biol* **1:** 179–186. doi:10.1038/35043058

Klaric JA, Wüst S, Panier S. 2021. New faces of old friends: emerging new roles of RNA-binding proteins in the DNA double-strand break response. *Front Mol Biosci* **8:** 668821. doi:10.3389/fmolb.2021.668821

Klec C, Prinz F, Pichler M. 2019. Involvement of the long noncoding RNA NEAT1 in carcinogenesis. *Mol Oncol* **13:** 46–60. doi:10.1002/1878-0261.12404

Langmead B, Salzberg SL. 2012. Fast gapped-read alignment with Bowtie 2. *Nat Methods* **9:** 357–359. doi:10.1038/nmeth.1923

Larsen DH, Poinsignon C, Gudjonsson T, Dinant C, Payne MR, Hari FJ, Rendtlew Danielsen JM, Menard P, Sand JC, Stucki M, et al. 2010. The chromatin-remodeling factor CHD4 coordinates signaling and repair after DNA damage. *J Cell Biol* **190:** 731–740. doi:10.1083/jcb.200912135

Lewis BA, Das SK, Jha RK, Levens D. 2023. Self-assembly of promoter DNA and RNA Pol II machinery into transcriptionally active biomolecular condensates. *Sci Adv* **9:** eadi4565. doi:10.1126/sciadv.adi4565

Liu N, Dai Q, Zheng G, He C, Parisien M, Pan T. 2015. N^6-methyladenosine-dependent RNA structural switches regulate RNA-protein interactions. *Nature* **518:** 560–564. doi:10.1038/nature14234

Liu Z, Ajit K, Wu Y, Zhu WG, Gullerova M. 2024. The GATAD2B–NuRD complex drives DNA:RNA hybrid-dependent chromatin boundary formation upon DNA damage. *EMBO J* **43:** 2453–2485. doi:10.1038/s44318-024-00111-7

Machour FE, Ayoub N. 2020. Transcriptional regulation at DSBs: mechanisms and consequences. *Trends Genet* **36:** 981–997. doi:10.1016/j.tig.2020.01.001

Marnef A, Legube G. 2021. R-loops as Janus-faced modulators of DNA repair. *Nat Cell Biol* **23:** 305–313. doi:10.1038/s41556-021-00663-4

Mattick JS, Amaral PP, Carninci P, Carpenter S, Chang HY, Chen LL, Chen R, Dean C, Dinger ME, Fitzgerald KA, et al. 2023. Long non-coding RNAs: definitions, functions, challenges and recommendations. *Nat Rev Mol Cell Biol* **24:** 430–447. doi:10.1038/s41580-022-00566-8

Mello SS, Sinow C, Raj N, Mazur PK, Bieging-Rollett K, Broz DK, Imam JFC, Vogel H, Wood LD, Sage J, et al. 2017. *Neat1* is a p53-inducible lincRNA essential for transformation suppression. *Genes Dev* **31:** 1095–1108. doi:10.1101/gad.284661.116

Michelini F, Jalihal AP, Francia S, Meers C, Neeb ZT, Rossiello F, Gioia U, Aguado J, Jones-Weinert C, Luke B, et al. 2018. From "cellular" RNA to "smart" RNA: multiple roles of RNA in genome stability and beyond. *Chem Rev* **118:** 4365–4403. doi:10.1021/acs.chemrev.7b00487

Pessina F, Giavazzi F, Yin Y, Gioia U, Vitelli V, Galbiati A, Barozzi S, Garre M, Oldani A, Flaus A, et al. 2019. Functional transcription promoters at DNA double-strand breaks mediate RNA-driven phase separation of damage-response factors. *Nat Cell Biol* **21:** 1286–1299. doi:10.1038/s41556-019-0392-4

Pisani G, Baron B. 2020. NEAT1 and paraspeckles in cancer development and chemoresistance. *Noncoding RNA* **6:** 43. doi:10.3390/ncrna6040043

Polo SE, Kaidi A, Baskcomb L, Galanty Y, Jackson SP. 2010. Regulation of DNA-damage responses and cell-cycle progression by the chromatin remodelling factor CHD4. *EMBO J* **29:** 3130–3139. doi:10.1038/emboj.2010.188

Quinlan AR, Hall IM. 2010. BEDTools: a flexible suite of utilities for comparing genomic features. *Bioinformatics* **26:** 841–842. doi:10.1093/bioinformatics/btq033

Raj N, Wang M, Seoane JA, Zhao RL, Kaiser AM, Moonie NA, Demeter J, Boutelle AM, Kerr CH, Mulligan AS, et al. 2022. The Mettl3 epitranscriptomic writer amplifies p53 stress responses. *Mol Cell* **82:** 2370–2384.e10. doi:10.1016/j.molcel.2022.04.010

Reynolds N, Salmon-Divon M, Dvinge H, Hynes-Allen A, Balasooriya G, Leaford D, Behrens A, Bertone P, Hendrich B. 2012. NuRD-mediated deacetylation of H3K27 facilitates recruitment of Polycomb repressive complex 2 to direct gene repression. *EMBO J* **31:** 593–605. doi:10.1038/emboj.2011.431

Smeenk G, van Attikum H. 2013. The chromatin response to DNA breaks: leaving a mark on genome integrity. *Annu Rev Biochem* **82:** 55–80. doi:10.1146/annurev-biochem-061809-174504

Smeenk G, Wiegant WW, Vrolijk H, Solari AP, Pastink A, van Attikum H. 2010. The NuRD chromatin-remodeling complex regulates signaling and repair of DNA damage. *J Cell Biol* **190:** 741–749. doi:10.1083/jcb.201001048

Taiana E, Favasuli V, Ronchetti D, Todoerti K, Pelizzoni F, Manzoni M, Barbieri M, Fabris S, Silvestris I, Gallo Cantafio ME, et al. 2020. Long non-coding RNA NEAT1 targeting impairs the DNA repair machinery and triggers anti-tumor activity in multiple myeloma. *Leukemia* **34:** 234–244. doi:10.1038/s41375-019-0542-5

Trifault B, Mamontova V, Cossa G, Ganskih S, Wei Y, Hofstetter J, Bhandare P, Baluapuri A, Nieto B, Solvie D, et al. 2024. Nucleolar detention of NONO shields DNA double-strand breaks from aberrant transcripts. *Nucleic Acids Res* **52:** 3050–3068. doi:10.1093/nar/gkae022

Ullah I, Thölken C, Zhong Y, John M, Rossbach O, Lenz J, Gößringer M, Nist A, Albert L, Stiewe T, et al. 2022. RNA inhibits dMi-2/CHD4 chromatin binding and nucleosome remodeling. *Cell Rep* **39:** 110895. doi:10.1016/j.celrep.2022.110895

Van Nostrand EL, Pratt GA, Shishkin AA, Gelboin-Burkhart C, Fang MY, Sundararaman B, Blue SM, Nguyen TB, Surka C, Elkins K, et al. 2016. Robust transcriptome-wide discovery of RNA-binding protein binding sites with enhanced CLIP (eCLIP). *Nat Methods* **13:** 508–514. doi:10.1038/nmeth.3810

Wen S, Wei Y, Zen C, Xiong W, Niu Y, Zhao Y. 2020. Long noncoding RNA NEAT1 promotes bone metastasis of prostate cancer through N6-methyladenosine. *Mol Cancer* **19:** 171. doi:10.1186/s12943-020-01293-4

West JA, Davis CP, Sunwoo H, Simon MD, Sadreyev RI, Wang PI, Tolstorukov MY, Kingston RE. 2014. The long noncoding RNAs NEAT1 and MALAT1 bind active chromatin sites. *Mol Cell* **55:** 791–802. doi:10.1016/j.molcel.2014.07.012

Yamazaki T, Souquere S, Chujo T, Kobelke S, Chong YS, Fox AH, Bond CS, Nakagawa S, Pierron G, Hirose T. 2018. Functional domains of NEAT1 architectural lncRNA induce paraspeckle assembly through phase separation. *Mol Cell* **70:** 1038–1053.e7. doi:10.1016/j.molcel.2018.05.019

Yang LZ, Wang Y, Li SQ, Yao RW, Luan PF, Wu H, Carmichael GG, Chen LL. 2019. Dynamic imaging of RNA in living cells by CRISPR–Cas13 systems. *Mol Cell* **76:** 981–997.e7. doi:10.1016/j.molcel.2019.10.024

Yankova E, Blackaby W, Albertella M, Rak J, De Braekeleer E, Tsagkogeorga G, Pilka ES, Aspris D, Leggate D, Hendrick AG, et al. 2021. Small-molecule inhibition of METTL3 as a

strategy against myeloid leukaemia. *Nature* **593:** 597–601. doi:10.1038/s41586-021-03536-w

Yap K, Chung TH, Makeyev EV. 2022. Hybridization-proximity labeling reveals spatially ordered interactions of nuclear RNA compartments. *Mol Cell* **82:** 463–478.e11. doi:10.1016/j.molcel.2021.10.009

Zhang W, Xie M, Shu MD, Steitz JA, DiMaio D. 2016. A proximity-dependent assay for specific RNA–protein interactions in intact cells. *RNA* **22:** 1785–1792. doi:10.1261/rna.058248.116

Zhang C, Chen L, Peng D, Jiang A, He Y, Zeng Y, Xie C, Zhou H, Luo X, Liu H, et al. 2020. METTL3 and N6-methyladenosine promote homologous recombination-mediated repair of DSBs

by modulating DNA–RNA hybrid accumulation. *Mol Cell* **79:** 425–442.e7. doi:10.1016/j.molcel.2020.06.017

Zhao Z, Sentürk N, Song C, Grummt I. 2018. lncRNA PAPAS tethered to the rDNA enhancer recruits hypophosphorylated CHD4/NuRD to repress rRNA synthesis at elevated temperatures. *Genes Dev* **32:** 836–848. doi:10.1101/gad.311688.118

Zong D, Oberdoerffer P, Batista PJ, Nussenzweig A. 2020. RNA: a double-edged sword in genome maintenance. *Nat Rev Genet* **21:** 651–670. doi:10.1038/s41576-020-0263-7

Zubradt M, Gupta P, Persad S, Lambowitz AM, Weissman JS, Rouskin S. 2017. DMS-MaPseq for genome-wide or targeted RNA structure probing in vivo. *Nat Methods* **14:** 75–82. doi:10.1038/nmeth.4057